

# Adaptive optics parallel spectral domain optical coherence tomography for imaging the living retina

Yan Zhang, Jungtae Rha, Ravi S. Jonnal, and Donald T. Miller

*School of Optometry, Indiana University, Bloomington, Indiana 47405*  
[yz7@indiana.edu](mailto:yz7@indiana.edu) and [jrha@indiana.edu](mailto:jrha@indiana.edu)

**Abstract:** Although optical coherence tomography (OCT) can axially resolve and detect reflections from individual cells, there are no reports of imaging cells in the living human retina using OCT. To supplement the axial resolution and sensitivity of OCT with the necessary lateral resolution and speed, we developed a novel spectral domain OCT (SD-OCT) camera based on a free-space parallel illumination architecture and equipped with adaptive optics (AO). Conventional flood illumination, also with AO, was integrated into the camera and provided confirmation of the focus position in the retina with an accuracy of  $\pm 10.3 \mu\text{m}$ . Short bursts of narrow B-scans ( $100 \times 560 \mu\text{m}$ ) of the living retina were subsequently acquired at 500 Hz during dynamic compensation (up to 14 Hz) that successfully corrected the most significant ocular aberrations across a dilated 6 mm pupil. Camera sensitivity (up to 94 dB) was sufficient for observing reflections from essentially all neural layers of the retina. Signal-to-noise of the detected reflection from the photoreceptor layer was highly sensitive to the level of ocular aberrations and defocus with changes of 11.4 and 13.1 dB (single pass) observed when the ocular aberrations (astigmatism, 3<sup>rd</sup> order and higher) were corrected and when the focus was shifted by 200  $\mu\text{m}$  (0.54 diopters) in the retina, respectively. The 3D resolution of the B-scans ( $3.0 \times 3.0 \times 5.7 \mu\text{m}$ ) is the highest reported to date in the living human eye and was sufficient to observe the interface between the inner and outer segments of individual photoreceptor cells, resolved in both lateral and axial dimensions. However, high contrast speckle, which is intrinsic to OCT, was present throughout the AO parallel SD-OCT B-scans and obstructed correlating retinal reflections to cell-sized retinal structures.

©2005 Optical Society of America

**OCIS codes:** (010.1080) Adaptive optics; (170.4500) Optical coherence tomography; (330.4460) Ophthalmic optics; (330.5370) Physiological optics; (330.4300) Noninvasive assessment of the visual system

---

## References and links

1. D. Huang, E. A. Swanson, C. P. Lin, J. S. Schuman, W. G. Stinson, W. Chang, M. R. Hee, T. Flotte, K. Gregory, C. A. Puliafito, and J. G. Fujimoto, "Optical coherence tomography," *Science* **254**, 1178-1181 (1991).
2. W. Drexler, U. Morgner, R. K. Ghanta, F. X. Kärtner, J. S. Schuman, and J. G. Fujimoto, "Ultrahigh-resolution ophthalmic optical coherence tomography," *Nature Med.* **7**, 502-507 (2001).
3. B. Cense, N. A. Nassif, T. C. Chen, M. C. Pierce, S. Yun, B. H. Park, B. E. Bouma, G. J. Tearney, and J. F. de Boer, "Ultrahigh-resolution high-speed retinal imaging using spectral-domain optical coherence tomography," *Opt. Express* **12**, 2435-2447 (2004), <http://www.opticsexpress.org/abstract.cfm?URI=OPEX-12-11-2435>.
4. M. Wojtkowski, V. J. Srinivasan, T. H. Ko, J. G. Fujimoto, A. Kowalczyk, and J. S. Duker, "Ultrahigh-resolution, high-speed, Fourier domain optical coherence tomography and methods for dispersion

- compensation," *Opt. Express* **12**, 2404-2421 (2004), <http://www.opticsexpress.org/abstract.cfm?URI=OPEX-12-11-2404>.
5. R. A. Leitgeb, W. Drexler, A. Unterhuber, B. Hermann, T. Bajraszewski, T. Le, A. Stingl, and A. F. Fercher, "Ultra-high resolution Fourier domain optical coherence tomography," *Opt. Express* **12**, 2156-2165 (2004), <http://www.opticsexpress.org/abstract.cfm?URI=OPEX-12-10-2156>.
  6. L. N. Thibos, X. Hong, A. Bradley, and X. Cheng, "Statistical variation of aberration structure and image quality in a normal population of healthy eyes," *J. Opt. Soc. Am. A* **19**, 2329-2348 (2002).
  7. R. K. Tyson, *Principles of Adaptive Optics* (Academic Press, New York, 1998).
  8. J. Liang, D. R. Williams, and D. T. Miller, "Supernormal vision and high resolution retinal imaging through adaptive optics," *J. Opt. Soc. Am. A* **14**, 2884-2892 (1997).
  9. H. Hofer, L. Chen, G. Y. Yoon, B. Singer, Y. Yamauchi, and D. R. Williams, "Improvement in retinal image quality with dynamic correction of the eye's aberrations," *Opt. Express* **8**, 631-643 (2001), <http://www.opticsexpress.org/abstract.cfm?URI=OPEX-8-11-631>.
  10. A. Roorda, F. Romero-Borja, W. J. Donnelly, H. Queener, T. J. Hebert, and M. C. W. Campbell, "Adaptive optics scanning laser ophthalmoscopy," *Opt. Express* **10**, 405-412 (2002), <http://www.opticsexpress.org/abstract.cfm?URI=OPEX-10-9-405>.
  11. D. T. Miller, J. Qu, R. S. Jonnal and K. Thorn, "Coherence gating and adaptive optics in the eye", in *Coherence Domain Optical Methods and Optical Coherence Tomography in Biomedicine VII*, V. V. Tuchin, J. A. Izatt, J. G. Fujimoto, eds., Proc. SPIE **4956**, 65-72 (2003).
  12. N. Ling, Y. Zhang, X. Rao, X. Li, C. Wang, Y. Hu, and W. Jiang, "Small table-top adaptive optical systems for human retinal imaging", in *High-Resolution Wavefront Control: Methods, Devices, and Applications IV*, J. D. Gonglewski, M. A. Vorontsov, M. T. Gruneisen, S. R. Restaino, R. K. Tyson, eds., Proc. SPIE **4825**, 99-108 (2002).
  13. M. Glanc, E. Gendron, F. Lacombe, D. Lafaille, J.-F. Le Gargasson, and P. Léna, "Towards wide-field retinal imaging with adaptive optics," *Opt. Comm.* **230**, 225-238 (2004).
  14. B. Hermann, E. J. Fernández, A. Unterhuber, H. Sattmann, A. F. Fercher, W. Drexler, P. M. Prieto, and P. Artal, "Adaptive-optics ultra-high-resolution optical coherence tomography," *Opt. Lett.* **29**, 2142-2144 (2004).
  15. B. Grajciar, M. Pircher, A. F. Fercher, and R. A. Leitgeb, "Parallel Fourier domain optical coherence tomography for in vivo measurement of the human eye," *Opt. Express* **13**, 1131-1137 (2005), <http://www.opticsexpress.org/abstract.cfm?URI=OPEX-13-4-1131>.
  16. Y. Zhang, J. Rha, R. S. Jonnal, and D. T. Miller, "Single shot retinal imaging with AO spectral OCT," in *Coherence Domain Optical Methods and Optical Coherence Tomography in Biomedicine IX*, V. V. Tuchin, J. A. Izatt, J. G. Fujimoto, eds. Proc. SPIE **5690**, 548-555 (2005).
  17. ANSI, *American National Standard for the Safe Use of Lasers, ANSI Z136.1* (Laser Institute of America, Orlando, FL, 2000).
  18. K. E. Thorn, J. Qu, R. J. Jonnal, and D. T. Miller, "Adaptive optics flood-illuminated camera for high speed retinal imaging," *Invest. Ophthalmol. Vis. Sci.* **44**, E-Abstract 1002 (2003).
  19. J. Hecht, *Understanding Fiber Optics* (Prentice Hall, New Jersey, 1998).
  20. W. Jiang and H. Li, "Hartmann-Shack wavefront sensing and control algorithm," in *Adaptive Optics and Optical Structures*, J. J. Schulte-in-den-Baeumen and R. K. Tyson, eds., Proc. SPIE **1271**, 82-93 (1990).
  21. J. Liang, B. Grimm, S. Goelz, and J. Bille, "Objective measurement of the wave aberrations of the human eye using a Hartmann-Shack wavefront sensor," *J. Opt. Soc. Am. A* **11**, 1949-1957 (1994).
  22. D. Malacara, *Optical Shop Testing 2<sup>nd</sup> ed.* (John Wiley & Sons, New York, 1992), 112-113.
  23. L. N. Thibos, X. Hong, A. Bradley, and R. A. Applegate, "Accuracy and precision of methods to predict the results of subjective refraction from monochromatic wavefront aberration maps," *J. Vis.* **4**, 329-351 (2004).
  24. R. Leitgeb, C. K. Hitzenberger, and A. F. Fercher, "Performance of Fourier domain versus time domain optical coherence tomography," *Opt. Express* **11**, 889-894 (2003), <http://www.opticsexpress.org/abstract.cfm?URI=OPEX-11-8-889>.
  25. R. J. Zawadzki, B. A. Bower, M. Zhao, M. Sarunic, S. Laut, J. S. Werner, and J. A. Izatt, "Exposure time dependence of image quality in high-speed retinal *in vivo* Fourier domain OCT," in *Ophthalmic Technologies XV*, F. Manns, P. G. Soederberg, A. Ho, B. E. Stuck, and M. Belkin, eds., Proc. SPIE **5688**, 45-52 (2005).
  26. C. A. Curcio, K. R. Sloan, R. E. Kalina, and A. E. Hendrickson, "Human photoreceptor topography," *J. Comparative Neurology* **292**, 497-523 (1990).
  27. D. R. Williams, "Topography of the foveal cone mosaic in the living human eye," *Vision Res.* **28**, 433-454 (1988).
  28. N. Nassif, B. Cense, B. H. Park, S. H. Yun, T. C. Chen, B. E. Bouma, G. J. Tearney, and J. F. de Boer, "*In vivo* human retinal imaging by ultrahigh-speed spectral domain optical coherence tomography," *Opt. Lett.* **29**, 480-482 (2004).
  29. B. Sander, M. Larsen, L. Thrane, J. L. Hougaard, and T. M. Jørgensen, "Enhanced optical coherence tomography imaging by multiple scan averaging," *Br. J. Ophthalmol.* **89**, 207-212 (2004).
  30. L. A. Riggs and J. C. Armington, J.C., "Motions of the retinal image during fixation," *J. Opt. Soc. Am.* **44**, 315-321 (1954).

## 1. Introduction

Microscopic imaging at the single cell level in the living human retina has attracted considerable attention in recent years as both vision and retinal disease fundamentally begin at the cellular level. Non-invasive observation of cells in their natural environment presents a new window of opportunity with enormous potential to address fundamental questions about vision as well as to provide earlier detection, better monitoring, and more effective treatment of retinal disease than could otherwise be realized. A leading imaging modality that approaches this goal is OCT, an interferometric imaging approach that provides very high sensitivity and axial resolution, making it particularly attractive for non-invasive imaging of the living retina [1]. Time domain OCT instruments including those with ultrahigh axial resolution ( $<3\ \mu\text{m}$ ) [2], however, fail to image individual cells in the living retina, owing to their slow speed (which leads to eye motion artifacts) and poor lateral resolution ( $>15\ \mu\text{m}$ ). Lateral resolution is limited by the small imaging pupil ( $<2\ \text{mm}$  at the eye) employed in these instruments.

Recently, Fourier domain OCT methods have demonstrated substantial increases in speed without loss in sensitivity compared to the more prevalent time domain embodiments [3-5]. Lateral resolution, however, remains poor as the same small pupils are used. While larger pupils could be employed to minimize diffraction, ocular aberrations dominate at larger pupil sizes and effectively mitigate any resolution benefit [6]. Conventional flood illuminated retina cameras and scanning laser ophthalmoscopes have overcome this resolution obstacle by employing adaptive optics technology [7] that compensates for the ocular aberrations. This has led to unprecedented lateral resolution approaching  $2\ \mu\text{m}$  and observations of single cells in the retina such as cone photoreceptors and blood cells [8-13]. Both camera types even with AO, however, remain poor at optical sectioning and the detection of weak retinal reflections in comparison to OCT.

More recently, AO has been combined with time-domain *en face* flood illumination (CCD-based) OCT and tomographic scanning OCT [11,14]. These efforts report lateral x axial resolutions of  $2\times 14\ \mu\text{m}$  and  $5-10\times 3\ \mu\text{m}$  in the eye, respectively. Differences in lateral resolution stem from differences in pupil size and effectiveness of the AO. Interestingly, the latter instrument demonstrated a 9 dB increase in signal-to-noise (SNR) when the aberrations, including noticeable defocus and astigmatism, across a 3.7 mm pupil were compensated for with AO. Neither AO-OCT camera provided observations of single cells in the living retina, being handicapped by the fundamental speed and sensitivity constraint imposed by the time-domain approach.

To this end we investigate a new type of retina camera that combines AO with SD-OCT. To increase speed further, SD-OCT was implemented for parallel imaging, in an approach similar to that recently employed for imaging the cornea and crystalline lens of the eye [15], but at a much higher frame rate (500 Hz). To our knowledge this is the first report in which parallel SD-OCT has been applied to imaging the living retina. Since coherence intrinsic to the OCT light source impedes accurate focusing, conventional flood illumination, also with AO, was integrated into the camera with the purpose of providing an independent and more accurate measure of the focus position in the retina. The AO parallel SD-OCT camera aimed to provide sufficient performance in 3D resolution, sensitivity, and speed to permit the observation of individual cells in the living human retina. In this paper, we compare retinal B-scans acquired on the same subject with the AO parallel SD-OCT, Stratus OCT3, and a research-grade scanning SD-OCT; quantitatively compare images of the photoreceptor mosaic acquired by AO parallel SD-OCT and conventional flood illumination at two retinal

eccentricities; present instrument sensitivity; quantify changes in SNR caused by shifts in focus and correction of the aberration pattern of the eye; and discuss limitations imposed by speckle. Early accounts of this work were presented at the 2005 SPIE Photonics West meeting [16].

## 2. Methods

### 2.1 Adaptive optics retina camera

A research-grade AO retina camera was developed for collecting high 3D resolution OCT and high 2D resolution conventional flood-illumination images of the microscopic retina in the living human eye. The camera consisted of four sub-systems: (1) parallel SD-OCT for B-scan imaging, (2) conventional flood illumination for *en face* imaging and focusing in the retina, (3) AO for compensation of the eye's wave aberrations, and (4) pupil retro-illumination and fixation channel for alignment of the subject's eye to the camera. Figure 1 shows conceptual and detailed layouts of the camera.

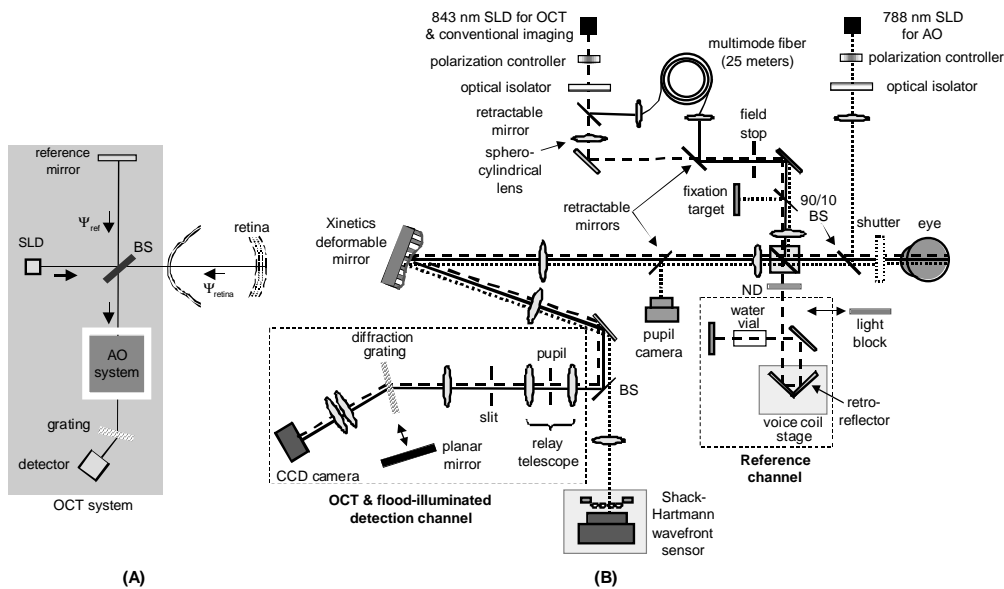


Fig. 1. (A) Concept layout shows the AO system as part of the SD-OCT detection channel. (B) Detailed layout of the AO parallel SD-OCT retina camera. The camera consists of four sub-systems. (1) AO system corrects the ocular aberrations using a 788 nm SLD, Shack-Hartmann wavefront sensor, and Xinetics deformable mirror (short dashed line). (2) Pupil retro-illumination and fixation channels permit alignment of the subject's eye to the retina camera. (3) Conventional flood-illumination is used to validate focusing in the retina and the physical size of microstructures in the retina (solid line). (4) Parallel SD-OCT acquires single shot B-scan images of the retina (long dashed line). Further details of the camera are given in the text.

The parallel SD-OCT system is based on a free-space Michelson interferometer design. Its illumination channel contains a 11 mW broadband superluminescent diode (SLD) ( $\lambda = 843$  nm,  $\Delta\lambda = 49.4$  nm) that is used in conjunction with a sphero-cylindrical lens for forming a line illumination pattern on the retina. The beam enters the subject's eye with a diameter of less than 2 mm. The reference channel contains a retroreflector mounted on a computer-driven voice coil translator (9 mm range in tissue) for controlling the reference optical path length and a 24 mm water vial for dispersion balancing the subject's eye. Light reflecting from the retina fills the pupil and is combined with the reference beam, the two forming superimposed line images at the 50  $\mu\text{m}$  slit (2.8  $\mu\text{m}$  at retina) in the detection channel. The slit is oriented

parallel to the line images. Upstream of the slit in the detection channel is an aperture that is conjugate to the pupil of the eye and is used to control the imaging pupil size, which in this experiment was set to 6 mm at the eye. Axial translation of the relay telescope permits focusing in the retina. Light passing through the slit is collimated by an achromat doublet and diffracted by a 1,200 lines/mm transmission grating (Wasatch Photonics) at Littrow's angle. Grating efficiency for the +1 order is 86% at 830 nm. Two achromat doublet lenses, designed for the near infrared band, focus the spectrally dispersed image onto a back-illuminated scientific-grade 12 bit CCD (Quantix:57, Roper Scientific, Inc.).

CCD read noise and pixel capacity for the two available CCD settings are 30.7/15.1 electrons root-mean-square (RMS) and 137,000/36,000 electrons, respectively. The setting with the larger pixel capacity was used for OCT and permitted photon limited imaging. The CCD array was 1056x530 pixels and consisted of a light-sensitive region of 512x530 pixels plus a similar storage area underneath the frame transfer mask. The predicted A-scan depth range is  $(\lambda^2/(4n_{retina}\Delta\lambda_{resol})) = 1$  mm with a useable range of about half this.  $n_{retina}$  is the gross refractive index of the retina (1.38), and  $\Delta\lambda_{resol}$  is the spectral resolution of the imaging spectrometer that was limited by the spectral width (0.125 nm) of a CCD pixel. As a first step, the power of the sphero-cylindrical lens was chosen so as to illuminate roughly a 100  $\mu$ m long line on the retina. 100 A-scans per B-scan permits the temporary storage of up to 10 B-scans on the CCD array before reading, and thus allows acquisition of a finite number of images at very high rates using the kinetics mode of the CCD, a method which we will refer to as short-burst imaging. Control software was developed that permits short-burst image acquisition rates of 500 Hz. For the latter, the exposure and delay durations were each 1 msec with eight images acquired in 15 msec. In order to obtain a measurement of the reference beam that is highly representative of the reference state during the actual retinal imaging (i.e., one that accounts for temporal fluctuations of the reference due to vibrations and temporal changes in the camera), the first image of each short burst sequence was that of the reference only. This was realized by timing a mechanical shutter, which was inserted in front of the eye (see Fig. 1), to momentarily close for just the first image of the burst sequence. Custom software was developed in Visual BASIC to acquire raw spectral images, subtract reference spectra, divide by the square root of the reference spectra (which removes irregularities in the illumination pattern), interpolate into  $k$ -space, balance dispersion using the foveal reflection [3], Fourier transform, and finally display the reconstructed B-scans of the retina.

Exposure level at the cornea for the 843 nm SLD was 1 mW, which illuminated an extended line of about 1/3 deg at the retina. This is more than an order of magnitude below the maximum permissible exposure for bursts of 1 msec pulses (8 in total) at 500 Hz as recommended by the American National Standards Institute (ANSI) [17].

With an earlier AO-OCT retina camera that we developed [11], spatial coherence of the SLD was found to generate noticeable speckle noise that masked visibility of microstructures in the retina and made focusing in the retina difficult. To avoid the focusing problem here, axial position of the focal plane in the retinal tissue was established using an incoherent flood-illuminated sub-system that captured *en face* images, for example of the cone mosaic or retinal capillary bed. Observation of these structures with the incoherent system confirms the plane of focus. Because focusing in the eye is sensitive to the light source spectrum (ocular chromatic aberrations) as well as the alignment of the camera components, the incoherent flood-illuminated system was integrated as much as possible with the parallel SD-OCT system. Specifically both imaging systems employed the same SLD, and their beams followed essentially identical paths, including that in the detection channel (see Fig. 1). This provided considerable assurance that both imaging systems were focused at the same retinal depth.

The light path for the incoherent sub-system is as follows. In the illumination channel, a motorized retractable mirror redirects light from the 843 nm SLD into 25 meters of multimode step index optical fiber (Lucent Technologies, Inc.). The fiber has a numerical aperture ( $NA$ ) of 0.22, core diameter of 105  $\mu$ m, and core refractive index ( $n_{core}$ ) of 1.457 at  $\lambda=0.633$   $\mu$ m. In

the fiber, the light is distributed among the fiber modes with modal dispersion causing each to propagate at different axial velocities. The 25 meters was of sufficient length to cause the time delay between exiting modes to be larger than the temporal coherence length of the SLD that effectively mitigated the source's spatial coherence (removes speckle) [18,19]. A second paper is in preparation that discusses the details of this multimode fiber illumination source.

Light exiting the fiber is redirected back into the system via a second motorized retractable mirror and into the subject's eye where it flood illuminates a one deg patch of retina. The flood illumination is centered on the line illumination of the parallel SD-OCT. The tip of the fiber is conjugate to the subject's retina. To avoid unwanted back reflections from the reference channel, a light block is physically inserted immediately upstream of the retro-reflector. In the detection channel, the slit and transmission grating are temporarily removed with the latter being replaced with a planar mirror that was carefully pre-aligned such that the reflected beam followed the same path as the +1 order of the diffraction grating. Insertion of the slit and interchange of the grating and planar mirror were realized using kinematic base plates. Precision of the plates was more than sufficient owing to the large diameter of the slit (50  $\mu\text{m}$ ) and the large axial magnification of the instrument (1 mm axial displacement at the Quantix CCD corresponds to 5.5  $\mu\text{m}$  at the retina). In this flood-illumination configuration, the Quantix 57 CCD captured aerial images of the retina whose acquisition was synchronized to the strobing SLD, realized by modulating the SLD current. Exposure duration, SLD intensity, and delay between consecutive images were computer controlled. Exposure level at the cornea for the 843 nm SLD was 0.73 mW (flood illumination), which illuminated a 1 deg patch of retina. This is more than 30 times below the maximum permissible exposure for individual 4 msec pulses and bursts of 4 msec pulses (8 in total) at 500 Hz as recommended by ANSI [17].

The AO system is an extension of that reported by Hofer, *et. al.* [9] with additional improvements and modifications necessary to operate simultaneously with OCT. It consists of a Shack-Hartmann wavefront sensor (SHWS) and deformable mirror (Xinetics, Inc.) that are controlled in closed loop via a desktop computer. The sensor employs a 0.75 mW pigtailed single mode SLD operating at 788 nm ( $\Delta\lambda= 20$  nm) that enters the subject's eye with a diameter less than 1 mm and is displaced from the corneal apex to avoid the bright corneal reflection. The beam focuses to a small spot on the retina that is roughly located at the geometric center of the parallel SD-OCT and conventional flood-illumination patterns. The reflected light fills the pupil of the eye and is distorted on passing back through the refracting media of the eye. A 17x17 lenslet array ( $f= 24\text{mm}$ ; lenslet dia. = 0.4mm), placed conjugate to the eye's pupil, samples the exiting wavefront across a 6.8 mm pupil. The array of focal spots produced by the lenslets is recorded with a scientific grade 12-bit CCD camera (CoolSNAP HQ, Roper Scientific, Inc.). The deformable mirror is positioned upstream of the lenslet array at a plane conjugate to the eye's pupil. The middle horizontal row of mirror actuators traverse 6.8 mm at the eye's pupil. The 37 lead magnesium niobate (PMN) actuators of the deformable mirror have a mechanical stroke of  $\pm 2$   $\mu\text{m}$ . A direct slope control method uses a single matrix multiplication operation to rapidly convert lateral shifts of the spots (local wavefront slopes) to voltages [20]. Artifacts from the edge actuators were avoided by imaging the retina through the central 6 mm of the pupil. The raw slope data were fit in real time to the derivatives of Zernike circle polynomials by the method of least squares described by Liang, *et. al.* [21]. These regression coefficients are used to represent the aberrated wavefront as a weighted sum of Zernike basis functions.

Custom dielectric beamsplitters were designed to reflect and transmit the corresponding wavelengths of the 843 nm and 788 nm SLDs. In addition, the 788 nm SHWS beacon is directed into the eye via a separate 90/10 pellicle to avoid back reflections from the reference channel. This allows simultaneous wavefront correction with conventional flood-illumination or parallel SD-OCT. The chromatic aberration of the eye caused a shift in defocus between

the two wavelengths that was offset by axially translating the relay telescope in the detection channel.

The AO operates at up to 22 wavefront measurements and corrections per second, although reduced rates of 6 and 14 Hz were used during parallel SD-OCT so as to lessen the probability of a wavefront correction coinciding with an OCT exposure as well as to permit additional diagnostic tools to run in the background. For consistency the same rates were used during conventional flood-illuminated imaging. While these slower rates are not optimal, it is well established that the dominant temporal components in the human eye's wave aberrations occur at low frequencies and the correction of these is typically sufficient for yielding sharp images of the cone mosaic and retinal capillary bed [9,11,18]. Exposure level at the cornea for the 788 nm SLD was 5  $\mu$ W, more than 117 times below the maximum permissible exposure for continuous intrabeam viewing recommended by ANSI [17].

As shown in Fig. 1, the AO system is positioned in the detection channel, downstream of both reference and sample channels. While a more straightforward approach may be to place the AO in the sample channel, the detection channel position offers several advantages. Specifically the uncommon path lengths (reference and sample channels) can be quite short (11 cm for the system in Fig. 1) and back reflections from the AO optics are unable to reach the SHWS sensor, which is highly sensitive to such reflections. Short uncommon paths promote interferometric stability, require few optical elements to be dispersion matched, and add little to the physical size of the camera (only a 11 cm reference channel is added). An obvious complication is that the AO acts on both sample and reference wavefronts thereby removing aberrations from the sample, but imparting the conjugate of the aberrations onto the reference. To prevent reference contamination, our approach was to design the detection channel as a point diffraction interferometer [22]. In this approach, the reference beam impinges on a confined central region of the corrector that is influenced at most by the middle five actuators, while the sample beam is exposed to all 37 actuators. This permits the reference beam to pass through the AO largely unaffected and the sample well compensated. To prevent dynamic changes in the middle five actuators from altering the reference, the middle five were frozen immediately after establishing a correction. Monitoring of the total RMS of the residual ocular wavefront aberrations before and after freezing the middle five actuators (the remaining 32 actuators continued to provide dynamic correction) revealed no appreciable increase in RMS (see Fig. 3). Thus this approach permits effective ocular wavefront correction with little compromise of the reference. A disadvantage of this approach is that the AO acts only on light exiting the eye and not that entering as well, and therefore the full gain in sensitivity that could be realized with AO is not attained. Conversely, the spatial resolution of the retinal image depends only on the light exiting the eye (and not that entering) and therefore is not compromised by this approach.

## 2.2 Human subject

Retinal images were collected on one subject (38 years of age) that was free of ocular disease and had normal corrected vision. Spectacle sphere and cylinder, which were obtained by a professional subjective refraction, were  $-2.25$  and  $-1.5$  diopters, respectively.

The subject's line of sight was centered along the optical axis of the retina camera with the aid of a fixation target, bite bar stage, and video camera that monitored the subject's pupil in retro-illumination. The fixation target was located at the subject's far point and consisted of high contrast cross hairs positioned on a rectilinear grid 0.5 deg apart. The target was back illuminated with uniform red light. As shown in Fig. 1, the target is positioned in the illumination channel and is therefore not viewed through the AO path. A dental impression attached to a sturdy xyz bite bar translation stage and a rigid forehead rest stabilized the eye and provided accurate pupil positioning. Retro-illumination of the pupil was realized with the 788 nm SLD.

The subject was mildly cyclopleged and his pupil dilated using two drops of Tropicamide 1% that were administered prior to measurements and one drop every hour thereafter. A single drop of Phenylephrine Hydrochloride 2.5% was also applied at the beginning of the measurements for additional dilation.

Refractive errors of sphere (defocus) and cylinder (astigmatism) were minimized in terms of the measured wavefront RMS by insertion of trial lenses at the spectacle plane. The trial lenses were slightly tilted so as to avoid their strong back reflection. Residual defocus and astigmatism associated with quantization of spectacle lens power (0.25 D) and subjective criterion for optimum focus in the presence of higher-order aberrations [23] were corrected with the AO system.

### 2.3 OCT sensitivity

Prior to retinal imaging, the sensitivity of the parallel SD-OCT system was measured by substituting a planar mirror for the eye in the sample channel. A neutral density filter with a single-pass attenuation of 2.5 ND was added to the sample channel to roughly mimic the total light loss in the eye. The exposure duration was 1 msec. The reference channel intensity was adjusted to fill the brightest CCD pixels to three quarters (103,000 electrons) of their maximum capacity (137,000 electrons). The slit was adjusted laterally to maximize throughput of the reference and sample beams. Sixteen CCD frames of the reference beam were captured and averaged. Then, interference spectra were recorded as the optical path length of the reference channel was incremented in 45  $\mu\text{m}$  steps via the voice coil stage across a range of 760  $\mu\text{m}$  (equivalent to 550  $\mu\text{m}$  in the retina). For each step, B-scans were reconstructed. Sensitivity was calculated for various A-scans along the B-scan and defined as the square of the signal amplitude divided by the variance of the noise floor [24]. The full-width-half-height (FWHH) of the axial point spread function (PSF) was also measured and converted to that in retinal tissue assuming a retinal refractive index ( $n_{\text{retina}}$ ) of 1.38.

### 2.4 Retinal imaging

Retinal images were collected on the subject using the following general protocol: (1) compensate ocular aberrations with trial lenses and AO, (2) focus the retina camera onto a specified retinal layer (e.g., cone photoreceptors) using the conventional flood-illuminated sub-system with dynamic correction, (3) convert camera from conventional flood illumination to parallel SD-OCT by removing the planar mirror, inserting the diffraction grating and slit, and lowering the two motorized retractable mirrors (conversion time is about 15 sec), and (4) acquire parallel SD-OCT images with dynamic correction. Steps (1) through (4) are repeated with the Xinetics mirror flat (without AO) and at different retinal locations.

More specifically, flood-illuminated and parallel SD-OCT images were acquired at 1 and 2.4 deg eccentricities along a radial line bisecting the superior retinal field. The retina camera was initially focused (using conventional imaging) on the photoreceptor layer, realized by acquiring images at discrete focus intervals of 1/36 diopters (10.3  $\mu\text{m}$  axial translation in the retina) across a depth range over which the cones could be coarsely observed (about 62  $\mu\text{m}$ ). The optimal focal location was defined as that providing the sharpest images of the cones. While at the optimal focus location for the photoreceptor layer, flood-illuminated and parallel SD-OCT images were acquired with and without AO compensation. In order to facilitate a fair comparison, the no-AO cases required re-focusing of the relay optics in order to account for the residual defocus that was no longer compensated for with the AO. For the 2.4 deg eccentricity, the camera was next refocused 200  $\mu\text{m}$  anterior to the cones, which corresponded roughly to 40  $\mu\text{m}$  immediately below the inner limiting membrane (ILM). Flood-illuminated and parallel SD-OCT images were again collected with and without AO compensation and with appropriate re-focusing of the optics.

Images of essentially the same patches of retina were also acquired with a commercial OCT (Stratus OCT3, Zeiss Meditec) and of roughly the same retinal eccentricities with a

fiber-based scanning SD-OCT, which did not contain AO. The scanning SD-OCT instrument was developed by Robert Zawadski and John Werner at the University of California at Davis and employed an 840 nm SLD ( $\Delta\lambda = 45$  nm) and a 2,048 pixel linescan camera (Atmel) [25]. Images from these established instruments were used to facilitate comparison with and validation of the AO parallel SD-OCT instrument. Specifically, a standard 5 mm (16.7 deg) B-scan, centered on the foveal pit, was collected along a radial line that bisected the superior and inferior retinal fields for the Stratus OCT3, and the nasal and temporal retinal fields for the scanning SD-OCT. While the scanning SD-OCT image was unfortunately along a meridian 90 degrees relative to the Stratus OCT3 and the AO parallel SD-OCT images, it still provides a benchmark to which AO parallel SD-OCT image quality can be compared. 1/3 deg (100  $\mu\text{m}$ ) subsections were then extracted at 1 and 2.4 deg eccentricity using the center of the fovea pit as the reference point.

### 3. Results and discussion

#### 3.1 OCT sensitivity and axial resolution

Figure 2 shows sensitivity of the parallel SD-OCT system obtained using a planar mirror and appropriate ND filters in place of the eye. Note the abscissa was rescaled for retinal tissue. Sensitivity is maximum (94 dB) for the central A-scan up to a depth of 185  $\mu\text{m}$  and decreases monotonically with tissue depth and location along the line illumination relative to the central A-scan. The middle  $\pm 25$  A-scans drop at a rate of roughly 2.1 dB/100  $\mu\text{m}$  of tissue and provide >90 dB sensitivity up to a depth of 363  $\mu\text{m}$ . The noticeable drop between the 25<sup>th</sup> and 50<sup>th</sup> A-scans is attributable to nonuniformities in the roughly Gaussian intensity profile of the 843 nm SLD and the sphero-cylindrical lens. The 75<sup>th</sup> A-scan is more than 20 dB below the central A-scan. While this drop is impractically large for retinal imaging due to the high loss of light in the eye, the results do illustrate that the instrument can acquire a single B-scan composed of 150 A-scans in 1 msec and achieve short burst rates of 75,000 A-scans/sec. These rates are 5 and 2.5 times higher than current SD-OCT retina cameras and could be more effectively realized in the eye if a more uniform illumination source with retinal irradiance comparable to the maximum of the current system were used.

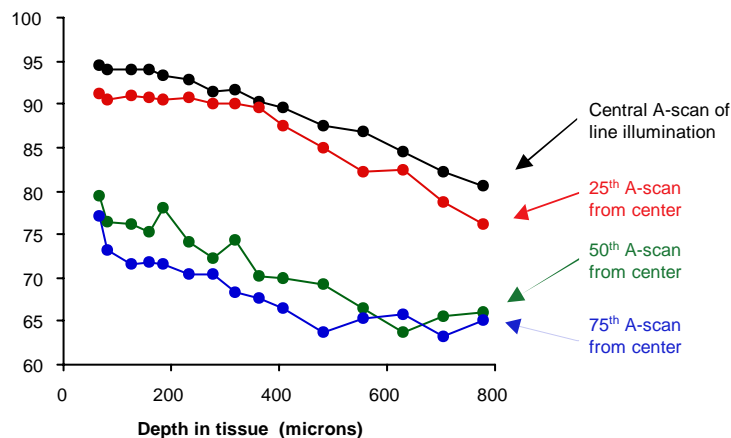


Fig. 2. Parallel SD-OCT sensitivity as a function of depth, converted from depth measured in air to tissue by using a refractive index of  $n = 1.38$ . The four A-scan locations are along the line illumination profile. A-scan location is in microns at the retina, e.g. the 25<sup>th</sup> A-scan is 25  $\mu\text{m}$  from the central A-scan.

The theoretical FWHH axial resolution ( $= 2\ln 2/\pi * \lambda_o^2/\Delta\lambda n_{retina}$ ) in retinal tissue for the 843 nm SLD is 4.6  $\mu\text{m}$ . The measured resolution obtained with the planar mirror in the

sample channel is 7.6  $\mu\text{m}$  (air), which corresponds to 5.5  $\mu\text{m}$  in the retina. Difference between theoretical and experimental values is likely due to residual dispersion mismatch and dependence of the SLD spectrum on output power, which was set below its maximum as a precautionary measure. In the retinal imaging experiments discussed further below, the specular ILM reflection at the base of the foveal pit was captured and used to determine an *in vivo* resolution of 5.7  $\mu\text{m}$ .

### 3.2 AO performance:

Image quality was assessed in terms of the root mean square (RMS) wavefront error and FWHH of the PSF. As an example, Fig. 3 shows traces of the total wavefront error for the one subject as measured by the SHWS before and during dynamic correction. Once initiated, full correction takes less than one second and typically reaches a mean corrected RMS of 0.08  $\mu\text{m}$ . Table 1 shows specific RMS error values measured during the retinal imaging experiment with and without AO correction. The error is displayed in terms of the total wavefront, individual 2<sup>nd</sup> order Zernike wavefronts, and the composite of 3<sup>rd</sup> order and higher. The left column depicts values that are typical of a good subjective refraction and the right represents a good correction. Note that the pre-corrected 2<sup>nd</sup> order Zernike coefficients correspond to equivalent sphere and cylinder refractive errors of  $-0.11$  and  $-0.26$  diopters, respectively. As indicated in the table, AO decreased the total RMS error by more than a factor of 8 with a residual corrected error of 0.08  $\mu\text{m}$ . For the experiments, the total RMS wavefront error during dynamic correction varied between 0.07 and 0.1  $\mu\text{m}$ , all of which produced a FWHH of the PSF of 3.0  $\mu\text{m}$ .

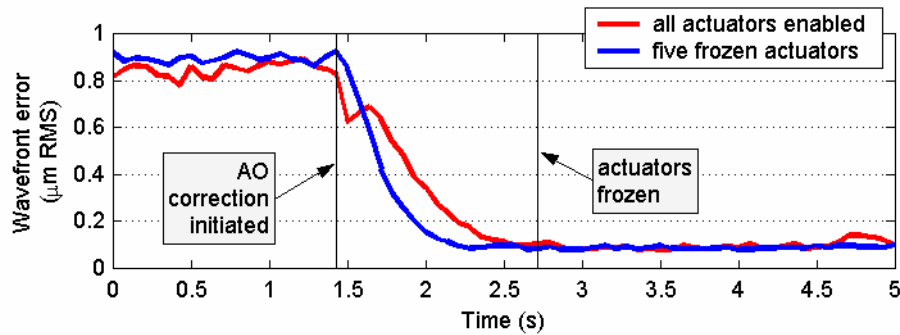


Fig. 3. Total wavefront error over time as measured by the SHWS before and during dynamic correction on one subject. The two traces depict correction with and without the middle five actuators frozen to a fixed correction (the remaining 32 actuators continued to provide dynamic correction). The time at which the actuators are frozen is indicated with no appreciable difference in the traces observed afterward.

Table 1. Measured wavefront aberrations across a 6.8 mm pupil for one subject with and without AO compensation. RMS wavefront error is shown for the total aberrations, Zernike defocus and astigmatism, and combined 3<sup>rd</sup> order and higher.

	Without AO compensation ( $\mu\text{m}$ )	With AO compensation ( $\mu\text{m}$ )
Total wavefront error	0.63	0.08
$Z_2^0$ (defocus)	0.39	0.00
$Z_2^{-2}$ (astigmatism, 45 deg)	0.04	0.00
$Z_2^2$ (astigmatism)	0.30	0.00
3 <sup>rd</sup> order and higher	0.40	0.08

### 3.3 Conventional flood illumination

The flood illuminated images shown in Fig. 4 represent well-focused cone images collected at each of two retinal eccentricities (1 and 2.4 deg) with and without AO. Defocus is less than 1/36 diopters for all four images as the collection protocol entailed adjusting focus in small increments of 1/36 diopters (10.3  $\mu\text{m}$ ) and selecting the visually clearest cone images. As a rule, a shift of 1/18 diopter (20.6  $\mu\text{m}$ ) from the position of clearest cones was found to reduce cone clarity, whose reduction could just be visually detected, and therefore defined the accuracy ( $\pm 10.3 \mu\text{m}$ ) of focus for this retinal layer. Cones at both eccentricities were observed over a focus range of approximately 62  $\mu\text{m}$ .

As evident in Fig. 4, some cone information is present without correction of the ocular aberrations (left column), but the mosaic is clearly of higher contrast and significantly better defined with correction (right column). As described below, AO parallel SD-OCT images (Figs. 6 to 8) were acquired from the central portion of these same retinal patches. To facilitate comparison, center-to-center cone spacing was directly measured from the central portion of the two AO compensated images in Fig. 4 and was 5.0 and 7.0  $\mu\text{m}$  at 1 and 2.4 deg, respectively. Average center-to-center spacing from anatomical studies of excised retina are 4.9 and 7.1  $\mu\text{m}$  for these same eccentricities [26].

It should be noted that resolution of the cone mosaic pattern requires that the fundamental spatial frequency that defines the mosaic is passed sufficiently by the system. As cones are largely arranged in a hexagonal matrix, their fundamental frequency is inversely related to the spacing of cone rows (= center-to-center spacing \*  $\cos 30^\circ$ ) [27] that corresponds to 3.9 and 6.2  $\mu\text{m}$  at 1 and 2.4 deg, respectively. Both are within the 3.0  $\mu\text{m}$  lateral resolution limit of our camera with AO.

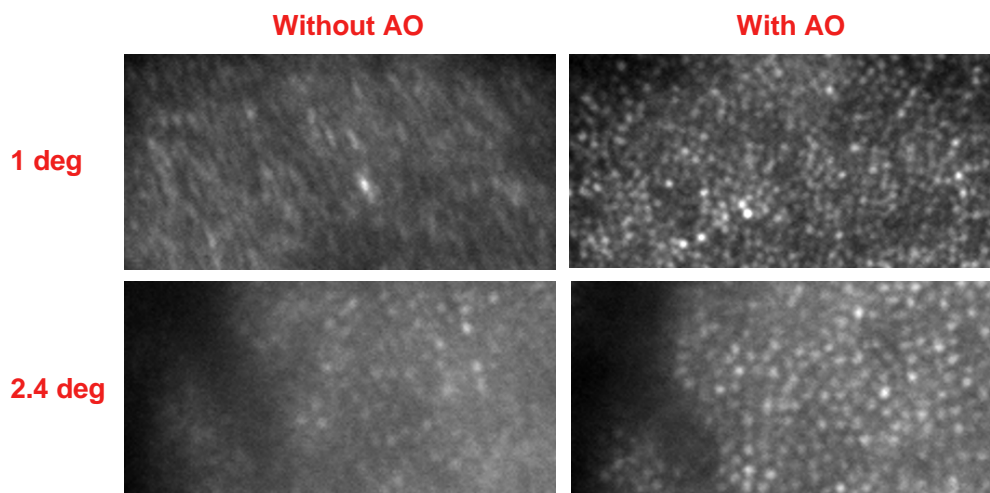


Fig. 4. Raw single cone images collected on the subject with the conventional flood-illuminated sub-system as depicted in Fig. 1. The four images represent the sharpest collected at each of two retinal eccentricities (1 and 2.4 deg) with and without AO. Images are 0.67x0.33 deg (200x100  $\mu\text{m}$ ) in size and were collected using the 843 nm SLD. Exposure duration was 4 msec, and imaging pupil size was 6 mm.

### 3.4 Conventional OCT

Figure 5 shows Stratus OCT3 and scanning SD-OCT B-scans that were collected along a radial line that bisected the foveal pit of one subject. Axial resolution of the Stratus and scanning SD-OCT instruments is 10 and 6  $\mu\text{m}$ , respectively. White rectangular boxes depict

100x560  $\mu\text{m}$  (width x height) subsections that are centered at 1 and 2.4 deg eccentricity and overlap with images collected with the AO parallel SD-OCT instrument on the same subject. Labels for the intra-retinal layers are also shown and depict current anatomical interpretation of high resolution OCT images [28]. Layers include the nerve fiber layer (NFL), ganglion cell layer (GCL), inner plexiform layer (IPL), inner nuclear layer (INL), outer plexiform layer (OPL), outer nuclear layer (ONL), junction between the inner and outer photoreceptor segments (IS/OS), and the retinal pigment epithelium (RPE). Most of the labeled layers are also suggested in the Stratus OCT3 image, but are not as well defined owing to the larger speckle [29].

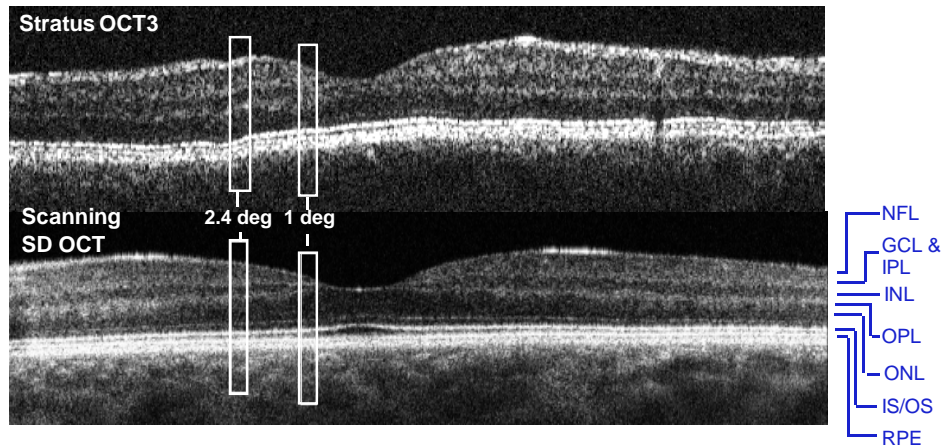


Fig. 5. (top) Stratus OCT3 and (bottom) scanning SD-OCT B-scans collected in the same subject. Images are centered on the fovea and bisect the superior and inferior retinal fields (Stratus OCT3), and nasal and temporal fields (scanning SD-OCT). B-scans are 4.9 mm (16.3 deg) wide and 0.75 mm in depth. White rectangles depict 100  $\mu\text{m}$  wide by 560  $\mu\text{m}$  deep subsections that are centered at 1 and 2.4 deg eccentricity and imaged with the AO parallel SD-OCT camera. A magnified view of these subsections is shown in Fig. 6 with the corresponding AO parallel SD-OCT B-scans.

### 3.5 AO parallel SD-OCT

Short-burst AO parallel SD-OCT videos were collected on one subject following the protocol outlined in the methods section. As a first step, we compared images from the videos to representative images acquired with the Stratus OCT3 and scanning SD-OCT (Fig. 5). Figure 6 shows four AO parallel SD-OCT images that were extracted from some of the best short burst videos (Fig. 8), i.e. videos that were sharpest about the intended plane of focus. While almost all of the videos revealed the retinal features contained in the best, many of them oscillated in brightness (discussed below) and were not considered. The images in Fig. 6 were acquired at two different retinal eccentricities (1 and 2.4 deg). Corresponding subsections of the Stratus OCT3 and scanning SD-OCT images (white rectangles in Fig. 5) are also shown.

Note that all B-scans in Fig. 6, including those of the Stratus and scanning SD-OCT, appear noticeably noisy, especially when visually compared to the full OCT images in Fig. 5. As the Stratus and scanning SD-OCT images in Fig. 6 are exact subsections copied from the images in Fig. 5, the apparent difference in noise results from the much higher display magnification of the Fig. 6 images; this higher magnification greatly enhances the visibility of the intrinsic speckle that is already present in the Fig. 5 images, but is too small to be observed at the scale used in Fig. 5.

The thickness of the retina (distance between ILM and posterior edge of cone outer segments) at 1 and 2.4 deg was measured at 267 and 329  $\mu\text{m}$  (Stratus OCT3), and 212 and 300  $\mu\text{m}$  (AO parallel SD-OCT), respectively. Measurements are in reasonable agreement, and

thickness differences of 20.6% and 8.8% relative to the Stratus are likely within the error due to image interpretation, sampling errors, and differences in retinal location. Thickness comparison with the scanning SD-OCT image was not performed as the latter was acquired from a different meridian, albeit at roughly the same eccentricity.

The images from the three cameras contain grossly similar bright and dark bands that occur at similar depths in the retina. Interestingly, the stratification of the intra-retinal layers appears most defined in the AO parallel SD-OCT images (left two columns) even though the AO parallel SD-OCT images are somewhat darker, which suggests a reduced signal-to-noise. While the layers are clearly less distinct than those in Fig. 5, they can be better visualized by compressing the AO parallel SD-OCT images along their lateral dimension to roughly that used in Fig. 5 and then digitally pasting together duplications of the AO parallel SD-OCT images to form a collage, an example of which is shown in Fig. 7. By simulating a larger field of view, the two collages (1 and 2.4 deg) more clearly show the stratification of the retina layers that is typically observed with high resolution OCT. Note the distinct physical separation between the inner nuclear layer and adjacent plexiform layers as well as the

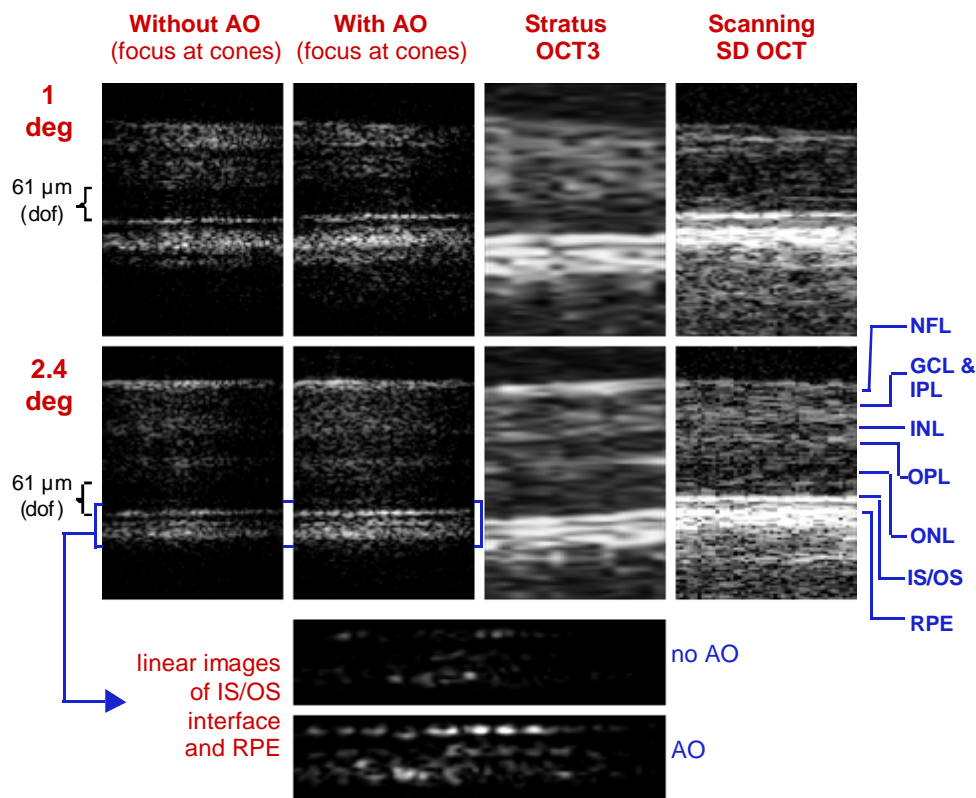


Fig. 6. (left two columns) B-scan images acquired with the AO parallel SD-OCT instrument in Fig. 2 with and without AO at 1 and 2.4 deg eccentricity (superior). (right two columns) Stratus OCT3 and scanning SD-OCT B-scans are shown at the same retinal eccentricities (from white rectangular boxes in Fig. 5). All images were acquired on the same subject and are 100  $\mu\text{m}$  wide and 560  $\mu\text{m}$  deep. (bottom) The interface between the inner and outer segments and RPE are enlarged and displayed as amplitude on a linear scale (as opposed to a log scale). Minor thresholding was used to enhance contrast. (far right) Labels for retinal layers are repeated from Fig. 5 and positioned where they should appear in the scanning SD-OCT image. Images without AO are normalized to the corresponding AO images, including the enlarged images. The apparent tilt in the Stratus OCT3 image at 2.4 deg is an eye motion artifact. The Stratus OCT3 images were acquired at 9.6  $\mu\text{m}/\text{A-scan}$  and interpolated (bicubic) to 1  $\mu\text{m}$ . The scanning SD-OCT images were acquired at 2  $\mu\text{m}/\text{A-scan}$  and interpolated (linear) to 1  $\mu\text{m}$ . The

2 and 9.6  $\mu\text{m}$  sampling intervals are noticeably smaller than their respective lateral resolutions.

Depth of focus (dof) is displayed at the left and defined in the text.

anterior (IS/OS junction) and posterior sides of the outer segments. The outer segments of photoreceptors are slightly longer at the smaller eccentricity as expected. Collectively, the results from Figs. 5 to 7 indicate the AO parallel SD-OCT instrument is sufficiently sensitive to detect reflections from essentially all major layers of the retina (NFL to retinal pigment epithelium (RPE)).

Figure 8 shows some of the best videos for the three imaging scenarios. Like the single B-scans shown in Fig. 6, bright localized reflections are observed at various depths in the thick retina. Certain reflections persist throughout the short burst videos and collectively move laterally and axially as a whole. This dynamic behavior, as revealed in the videos, suggests these are reflections from tissue rather than some sort of artifacts due to noise, retina motion, or changes in illumination. Some of the dimmer reflections that fluctuate rapidly and randomly in intensity are likely noise, however, the bright ones (which are clearly above the noise floor) reveal dynamic changes in the retina that occur on the scale of milliseconds. Movement of the retina across the 5-burst videos (9 msec) is relatively small and suggests that motion within individual exposures (1 msec) is largely negligible compared to the size of single cells. This observation qualitatively agrees with spatial and temporal measurements of involuntary movement of the retina for a fixating eye [30]. It is also consistent with observations with the well established AO flood-illuminated retina camera at the University of Rochester [9] whose exposures times are four times longer (4 msec) than the 1 msec used here.

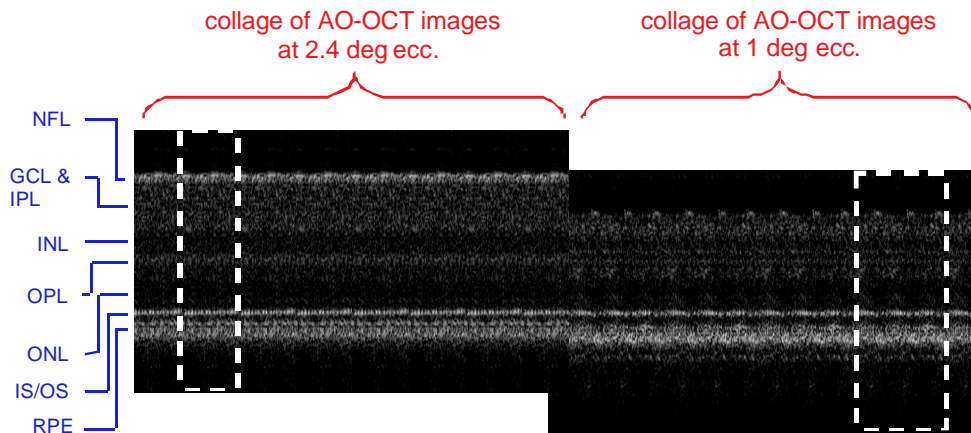


Fig. 7. Two collages created by digitally pasting together an alternating sequence of AO parallel SD-OCT images acquired at 1 and 2.4 deg eccentricity. The collages are roughly 3.25 to 3.5 degrees wide. Focus is at the cones. Each set of images was taken from the same short burst videos. The collage at 2.4 deg eccentricity was generated from two images (each 70 A-scans from the central region of a B-scan; dashed white rectangle represents the combined two images and is 140 A-scans) that were repeated about 7 times. The collage at 1 deg eccentricity contains three images (each  $\sim 70$  A-scans; dashed white rectangle represents 210 A-scans) that were repeated about 5 times. The collages were axially registered to each other by aligning the reflection from the IS/OS segment. Note the enhanced clarity of the major retinal layers compared to that for the highly magnified and narrow AO parallel SD-OCT images in Fig. 6.

Some of the videos unfortunately oscillate in brightness; these oscillations occur randomly and are most likely an artifact of a mechanical vibration in the AO parallel SD-OCT instrument (e.g., mechanical shutter, deformable mirror) that momentarily reduces the contrast of the information-bearing optical fringes at the CCD. We know these oscillations do not originate in the SLD light source or Quantix CCD detector as the same source and detector are

used for the conventional flood illumination sub-system and no such fluctuations were observed with this latter sub-system.

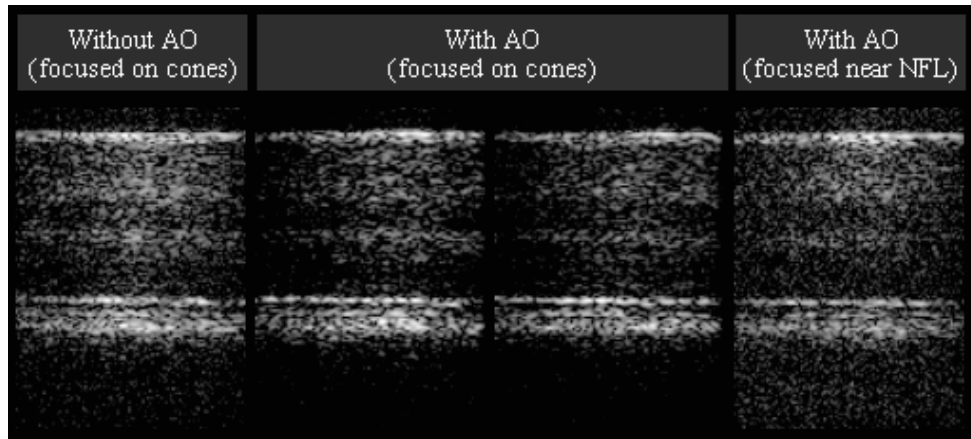


Fig. 8. Five-burst B-scan videos collected of the same patch of retina at 2.4 deg eccentricity for three scenarios: (left) focused on the cones and without AO, (middle) focused on the cones and with AO; (right) focus shifted anteriorly 200  $\mu\text{m}$  and with AO. Note that the physical separation between the ILM (upper edge of the topmost bright layer) and anterior side of the photoreceptor outer segments (segmented bright line in lower half) is around 272  $\mu\text{m}$ . Each B-scan is composed of 100 A-scans spaced 1  $\mu\text{m}$  apart. Videos were captured at 500 Hz with 1 msec exposure and run at 4 Hz, which is 125 times slower than the actual acquisition rate. The videos are best viewed in “loop” mode.

Speckle is an unfortunate byproduct of the interferometric nature of OCT and is indeed readily visible in the images acquired from all three instruments (Figs. 5 to 8). For the AO parallel SD-OCT images, it clearly obstructs correlating retinal reflections to microscopic retinal structures, especially those that approach the size of individual speckle. Speckle in the AO parallel SD-OCT images is about the average size predicted by theory (2.9 and 5.7  $\mu\text{m}$  in X and Z, respectively) for the imaging configuration used here. That is, the lateral dimension is given by the diffraction-limited spot size and the axial dimension by the OCT resolution. As evident in Fig. 6, the commercial and research-grade OCT instruments generate speckle of noticeably different size and shape. For example, speckle in the commercial OCT images has lateral and axial dimensions of about 20 and 10  $\mu\text{m}$ , respectively, which is significantly larger than that in the AO parallel SD-OCT images. Speckle in the scanning SD-OCT images has lateral and axial dimensions of about 10 and 6  $\mu\text{m}$ , respectively. The axial size of this speckle is comparable to that of the AO parallel SD-OCT; its lateral size, however, is noticeably larger. These differences in size and shape result from differences in the pupil (1 and 6 mm) and coherence lengths of the SLD light sources ( $\sim 10$  and 5.7  $\mu\text{m}$ ). In Fig. 6, smaller speckle appears clearly less disruptive of retinal features and illustrates an advantage of larger pupils and shorter coherence length sources. However, even with the large 6 mm pupil and 5.7  $\mu\text{m}$  coherence length of the AO parallel SD-OCT instrument, our results show that fully developed speckle is still present and substantially limits the microscopic retinal structures we can observe even though the instrument has achieved the necessary 3D resolution, sensitivity, and speed required to observe these structures.

While speckle is clearly disruptive, some microscopic structures are apparent particularly within the depth of focus when it is positioned where cones are clearest in flood illumination. Depth of focus is about 61  $\mu\text{m}$  and is defined as two times the Rayleigh range for a Gaussian beam and a 6 mm pupil (see Fig. 6). Specifically the bright reflection from the interface between the inner and outer segments of the photoreceptors appears spatially segmented

having a quasi-regular pattern with a periodicity of several microns. This unique pattern was not observed in any of the other retinal layers for any of the OCT images collected. Interestingly, this quasi-regular pattern largely (but not completely) disappears into a thin line when there is no AO correction (Fig. 6; Fig. 8, left video) or when the focus is shifted to another plane in the retina away from the cones (Fig. 8, right video). The presence of some pattern information without AO should be expected as the cone mosaic pattern is partially visible without AO for conventional flood illumination (see Fig. 4). Note that the visibility of the cone mosaic in the flood illumination images without AO is fairly typical for subjects with normal optical quality when defocus and astigmatism are meticulously corrected as was done here. An enlarged view of the RPE and interface between the inner and outer segments is shown at the bottom of Fig. 6. While both enlarged images appear to contain cone structural information, only the AO image contains a regular spacing ( $\sim 7 \mu\text{m}$ ) that matches that measured with flood illumination (Fig. 4). The structural spacing without AO is noticeably smaller suggesting it is corrupted by speckle, whose average size is similar to the spacing. We have ruled out the origin of the regular pattern being a post-processing artifact as reflective structures visible at other depths in the retina do not share the same regular characteristic. Note the increased brightness of the IS/OS interface and to a lesser extent the RPE when the aberrations are compensated. This is particularly evident in the enlarged amplitude images of Fig. 6 and would be even more dramatic if displayed as intensity on a linear scale.

In the Stratus OCT3 and scanning SD-OCT images (Figs. 5 and 6), the reflection from the inner/outer segment junction appears as a solid line with no evidence of a regular pattern. This result is in agreement with the OCT literature.

The sharpest cone images in flood illumination presumably occur with the focus at the anterior tips of the inner segments. It is interesting then that the reflection from the junction between the inner and outer segments as well as a suggestive one near the posterior side of the outer segment (e.g. third video from the left in Fig. 8) appear spatially segmented (i.e., in focus) with a periodicity of several microns. We suspect these intra-photoreceptor layers, albeit strictly out of focus, are indeed optimally focused owing to the waveguide nature of the photoreceptors. Confirmation will require meticulously focusing deeper into the photoreceptors, which we have not yet done. These results suggest that AO-OCT might be the right tool to do a comprehensive study of photoreceptor waveguide properties in a way not previously possible.

If the quasi-regular pattern observed in the reflection from the inner/outer segment junction corresponds to the spacing of cone photoreceptors, the periodicity of the pattern should match that of the photoreceptors, which varies with retinal eccentricity. In Fig. 6, the AO-corrected image at 1 deg suggests a finer spacing in the patterned reflection than that at 2.4 deg. To help quantify this apparent difference, Fig. 9 plots lateral cross sections through the B-scans at the depth of the inner/outer segment reflection. From Fig. 9, the spacing between adjacent bright reflections in those portions that reveal a clear periodicity is 5.2 and 6.9  $\mu\text{m}$  at 1 and 2.4 deg eccentricity, respectively, which reasonably matches the center-to-center cone spacing directly measured in the flood-illuminated images in Fig. 4. Obviously, the cross sectional plots are somewhat difficult to interpret due to the fact that the 2.8  $\mu\text{m}$  slit samples a photoreceptor mosaic that is at best hexagonally packed with local inhomogeneities in the receptor distribution. Moreover, eye motion causes the mosaic to randomly shift relative to the slit position. As indicated in the figure caption, cones centered on the slit should produce well defined reflectance profiles that are insensitive to eye motion perpendicular to the slit and smaller than a cone diameter. However, cones bisected by the edge of the slit are more likely to appear merged with adjacent cone profiles, which also fall under the slit, with small eye motion perpendicular to the slit causing noticeable changes in the profile shape (see arrows in Fig. 9.)

It is for these reasons that the Fig. 9 plots likely do not show a well defined periodic array that extends across the entire length of the slit, but rather evidence of one confined to small

sections. Indeed, the black arrows in Fig. 9 indicate possible centers of cones whose profiles are stable between frames. The gray arrows on the other hand reveal, what we believe to be, the edges of cones whose profiles gradually morph from one frame to the next as retina motion causes the slit to sample slightly different patches of retina for each frame. As can be seen in the sequence of frames (1, 5, and 7), the reflectance profiles of some individual cones change, decreasing and increasing in brightness as well as separating and joining with those of neighboring cones. These changes are not large as the 500 Hz burst rate of the frames effectively mitigates most eye motion.

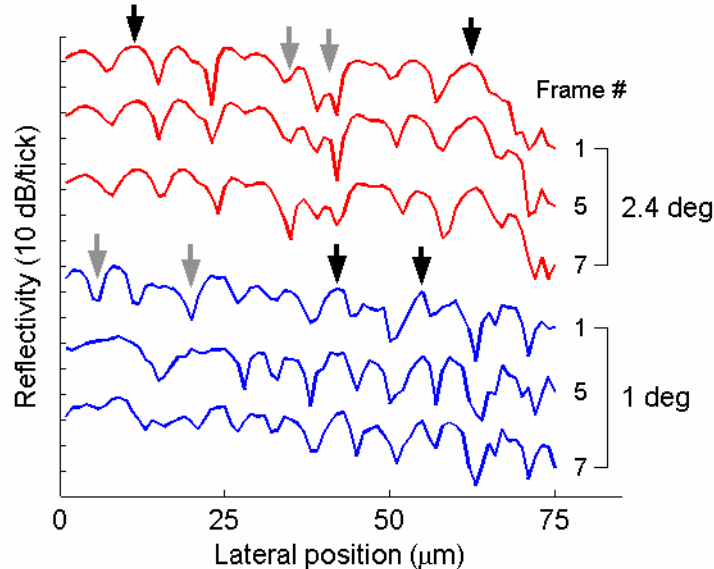


Fig. 9. Lateral reflectance profiles through the elongated structures (photoreceptor outer segments) for AO-corrected B-scan images at 2.4 (red) and 1 (blue) deg eccentricities for two short-burst sequences. Frame numbers correspond to the temporal sequence within a single short-burst series where frames 1, 5, and 7 are separated by 8 and 4 msec, respectively. Profiles are shifted vertically in the plot to facilitate visual comparison. Black arrows indicate the centers of cones whose profiles are stable between frames and insensitive to small retinal motion perpendicular to the slit. Gray arrows indicate the edges of cones and reveal the apparent separation or merging of adjacent cones due to retinal motion perpendicular to the slit. Retinal motion parallel to the slit causes a shift in the entire profile.

The strength of our interpretation of the B-scan cross sections in Fig. 9 is weakened by the unavoidable subjectivity inherent in the analysis. For a more objective comparison of cone spacing that takes into account all information captured by the slit, we analyzed both flood illuminated and OCT data in the Fourier domain [31]. To account for the pseudo-hexagonal distribution of the cones and the random position of the narrow slit at the cones due to eye motion, the  $2.8 \times 100 \mu\text{m}$  slit was projected onto the 1 and 2.4 deg flood illumination cone images and from which 1D power spectra were computed along the slit length using only the narrow slice of the mosaic sampled by the slit. Because only the general location is known at which the slit sampled the retinal patch in the actual AO parallel SD-OCT experiment, a rolling average of the power spectra was computed. This was realized by laterally shifting the slit across the portion of each cone mosaic image (Fig. 4) where it was known to fall. The resultant power spectra (black, dashed) are shown in the three plots of Fig. 10 for the two eccentricities. Note cusps in the spectra occurring at frequencies corresponding to 5 and  $7.1 \mu\text{m}$  for the 1 and 2.4 deg eccentricity, respectively. Power spectra (left) generated from the OCT images are also shown for cross sectional slices through the interface between the inner and outer segments, outer plexiform layer, outer nuclear layer, and inner plexiform layer. As

the figure reveals, only the OCT cone curve contains noticeable energy localized at the spatial frequency corresponding to  $7\ \mu\text{m}$ , which reasonably agrees with the  $7.4\ \mu\text{m}$  predicted from conventional flood illumination. The middle and right power spectra plots in Fig. 10 show the impact of AO at both 1 and 2.4 deg eccentricity when focused on the cones. Spectra were averaged across seven B-scans for each of the two eccentricities. Cusps in the power spectra are again observed with peaks at  $5.2$  and  $7\ \mu\text{m}$ , which are in agreement with that predicted by the flood-illuminated images. While the cusps are sufficiently well defined for the purposes of our comparison, the visually clear periodicity in the mosaic images of Fig. 4 and OCT images of Fig. 6 suggests that they should be more prominent. We surmise that this is due to local disruptions in cone periodicity in conjunction with a fundamental sampling limitation in which the slit falls across cone centers and edges (see gray arrows in Fig. 9).

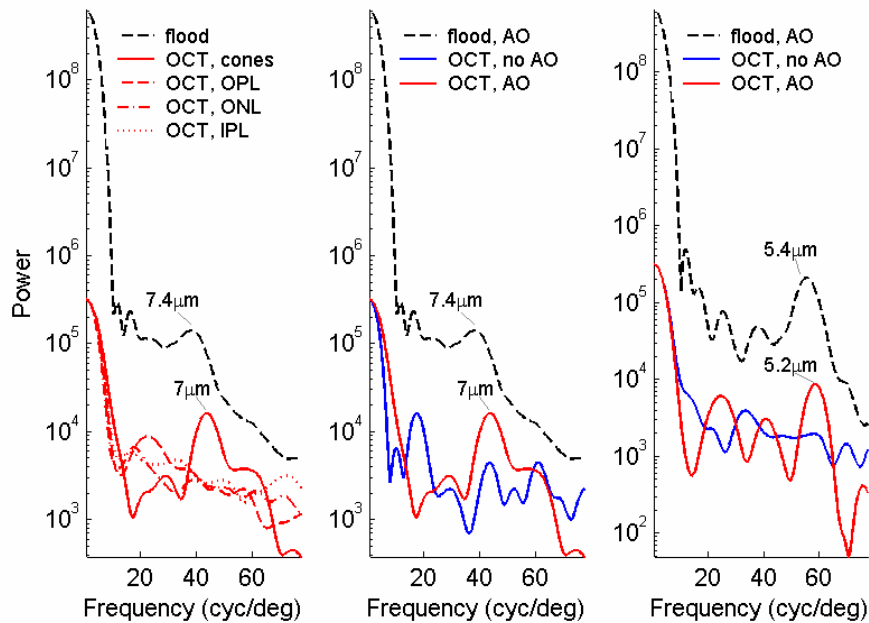


Fig. 10. Average power spectra obtained by 1D Fourier transformation (black dashed curves) of the conventional flood illuminated AO images in Fig. 4 after being sampled by the  $2.8 \times 100\ \mu\text{m}$  slit and (red and blue curves) of cross sectional slices through the interface between the inner and outer segments, outer plexiform layer, outer nuclear layer, and inner plexiform layer. (left) Power spectra are shown for different depths in the retina at the 2.4 deg eccentricity. (center and right) Power spectra are shown with and without AO at eccentricities of 2.4 and 1 degrees, respectively. All parallel SD-OCT curves are normalized to have the same power at 0 cyc/deg.

The gain in spatial resolution afforded by AO should also be accompanied by a gain in SNR as correction of the ocular aberrations permits a more concentrated focus of the retinal reflection at the CCD detector. The change in the SNR of the photoreceptor and nerve fiber layer (NFL) reflectance were studied for three imaging scenarios: (1) focus at the cones without AO correction, (2) focus at the cones with AO dynamic correction, and (3) focus near, but not at, the NFL with AO dynamic correction. The same 2.4 deg retinal patch was imaged in all three scenarios. To reduce speckle contamination that would lead to a wrong comparison, 20 contiguous A-scans from each short burst image were averaged and from which SNR of cones and NFL ( $SNR_{\text{cone\_typical}}$  and  $SNR_{\text{NFL\_typical}}$ , respectively) were calculated. Figure 11 shows typical profiles (average of 20) for the three scenarios. Note that comparing the SNR visually from Fig. 11 does not precisely reflect the true trend because of differences in the noise floor in these profiles, though they differ by less than 1.3 dB.

Table 2 lists  $SNR_{cone\_typical}$  and  $SNR_{NFL\_typical}$  for the three imaging scenarios. The table shows, as expected, that the detected retinal reflection is highly dependent on focus and ocular aberrations. For example, a 11.4 dB increase in  $SNR_{cone\_typical}$  is observed when the ocular aberrations are compensated for with dynamic AO. This increase reflects the influence of the correction of 0.50  $\mu\text{m}$  RMS wavefront error (astigmatism, 3<sup>rd</sup> order and higher) by AO. It is expected that there will be an additional increase in  $SNR_{cone\_typical}$  if AO acts on both the light entering and exiting the eye instead of only the latter, as in this AO parallel SD-OCT camera. It is also worth pointing out that there is a 13.1 dB drop of SNR in  $SNR_{cone\_typical}$  when the focus is shifted from the layer at which clearest flood-illumination images of cones were acquired to a layer 200  $\mu\text{m}$  anterior (0.55 diopters of defocus), in the presence of dynamic AO correction. This decrease in SNR was due to 0.55 diopter defocus since AO was dynamically correcting the ocular aberration during the experiment. From a theoretical standpoint, light efficiency through the OCT slit is predicted to decrease by 12.3 dB when 0.55 diopters of defocus are added and the system is assumed diffraction-limited for a 6 mm pupil. The NFL and outer nuclear layer also show consistent differences in reflectivity associated with focus and AO correction, although to a lesser extent. One would expect similar changes for the plexiform layers, but this was not observed. Perhaps this is because the plexiform layers partially straddled the two focus positions considered here and therefore received no net benefit from AO. This latter observation will require further investigation. Lastly, it is interesting to note that the signal from the NFL decreases when AO is turned on, and the light is focused at the photoreceptors. We believe this because AO reduces the depth of focus. To substantiate this, optical point spread functions were derived from the corresponding SH wavefront measurements with and without AO and in the presence of 2.9  $\mu\text{m}$  of defocus. This amount of defocus corresponds to the axial distance between the focal plane (anterior tip of the cone inner segments) and the NFL. The calculations predict that noticeably more light from the NFL will pass through the imaging spectrometer slit without AO than with AO when light is focused on the photoreceptors. This result is consistent with our experimental findings.

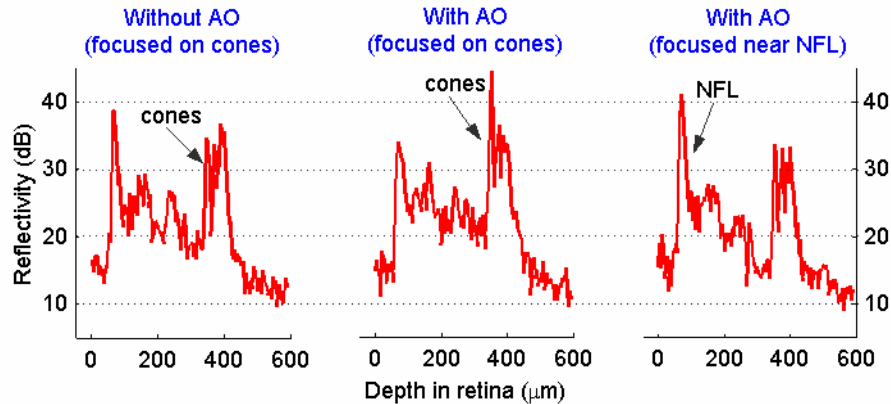


Fig. 11. Average profile of 20 contiguous A-scans centered about the brightest region in the B-scan for each of the three imaging scenarios shown in Fig. 8. Images were obtained at 2.4 deg retinal eccentricity.

Table 2. Average SNR for cones and NFL for three imaging scenarios as described in the text.

	Without AO (focused on cones)	With AO (focused on cones)	With AO (focused near NFL)
$SNR_{NFL\_typical}$ (dB)	44.4	41.3	46.4
$SNR_{cone\_typical}$ (dB)	40.5	51.9	38.8

#### 4. Conclusion

While OCT instruments have advanced considerably in the last 15 years, none have reported images showing single cells in the living human retina, even with ultrahigh axial resolution OCT ( $< 3 \mu\text{m}$ ). To this end we have successfully developed a parallel SD-OCT camera that is equipped with AO as well as an AO conventional flood-illuminated sub-system. The camera was found to have sufficient 3D resolution ( $3.0 \times 3.0 \times 5.7 \mu\text{m}$ ), sensitivity (up to 94 dB), and speed (100 A-scans/msec for single shot) for imaging the retina at the single cell level. The camera provided first observations of the interface between the inner and outer segments of individual cones, resolved simultaneously in both lateral and axial dimensions. Camera sensitivity was sufficient for observing reflections from essentially all neural layers of the retina. Signal-to-noise of the detected reflection from the photoreceptor layer was highly sensitive to the level of ocular aberrations and defocus with changes of 11.4 and 13.1 dB (single pass) observed when the ocular aberrations (astigmatism, 3<sup>rd</sup> order and higher) were corrected and when the focus was shifted by 0.54 diopters in the retina, respectively.

A critical limitation of the current AO SD-OCT instrument is high contrast speckle noise that is present throughout the retinal image, undermines the resolution and contrast benefits of AO, and obstructs correlating retinal reflections to specific cell-sized retinal structures. While speckle is a serious problem, a meaningful solution will permit OCT to reap the full benefit of AO that conventional flood illumination and scanning laser ophthalmoscopy now enjoy, but with the additional benefits of considerably higher axial resolution and sensitivity. The AO parallel SD-OCT results presented here already reveal sub-cellular structure in the cone photoreceptor layer that have not been reported with either flood illumination or SLO systems. These first results will surely improve as speckle reduction techniques are applied and real-time 3D imaging is implemented.

#### Acknowledgments

The authors thank Thomas Milner, Robert Zawadski, Jack Werner, Barry Cense, Weihua Gao, and Arthur Bradley for advice on the project as well as previous group members Karen Thorn, Junle Qu, and Huawei Zhao. Assistance from Marcos van Dam and David Williams' group with the adaptive optics system is much appreciated. The authors also thank William Monette and Daniel Jackson's group for electronics and machining support. Financial support was provided by the National Eye Institute grant 5R01 EY014743. This work was also supported in part by the National Science Foundation Science and Technology Center for Adaptive Optics, managed by the University of California at Santa Cruz under cooperative agreement No. AST-9876783.